Journal of Magnetic Resonance 213 (2011) 14–21

Contents lists available at ScienceDirect

Journal of Magnetic Resonance

journal homepage: www.elsevier.com/locate/jmr

Band-selective chemical exchange saturation transfer imaging with hyperpolarized xenon-based molecular sensors

Tyler Meldrum [a,c], Vikram S. Bajaj [a,c,*], David E. Wemmer [b,c], Alexander Pines [a,c]

[a] Materials Sciences Division, Lawrence Berkeley National Laboratory, Berkeley, CA 94720, USA
[b] Physical Biosciences Division, Lawrence Berkeley National Laboratory, Berkeley, CA 94720, USA
[c] Department of Chemistry, University of California, Berkeley, CA 94720, USA

ARTICLE INFO

Article history:
Received 27 June 2011
Available online 13 July 2011

Keywords:
MRI
Contrast agent
Chemical exchange saturation transfer
Xenon
Hyperpolarization

ABSTRACT

Molecular imaging based on saturation transfer in exchanging systems is a tool for amplified and chemically specific magnetic resonance imaging. Xenon-based molecular sensors are a promising category of molecular imaging agents in which chemical exchange of dissolved xenon between its bulk and agent-bound phases has been use to achieve sub-picomolar detection sensitivity. Control over the saturation transfer dynamics, particularly when multiple exchanging resonances are present in the spectra, requires saturation fields of limited bandwidth and is generally accomplished by continuous wave irradiation. We demonstrate instead how band-selective saturation sequences based on multiple pulse inversion elements can yield saturation bandwidth tuneable over a wide range, while depositing less RF power in the sample. We show how these sequences can be used in imaging experiments that require spatial–spectral and multispectral saturation. The results should be applicable to all CEST experiments and, in particular, will provide the spectroscopic control required for applications of arrays of xenon chemical sensors in microfluidic chemical analysis devices.

1. Introduction

Molecular imaging promises minimally invasive and anatomically specific localization of chemical phenomena in morphologically detailed magnetic resonance images. This presents obvious applications to early detection of pathological states in living organisms, but can also be applied to chemical and biochemical profiling of complex mixtures [1]. Molecular imaging contrast agents for both applications are commonly molecular or supramolecular assemblies that couple a contrast center, which perturbs a magnetic resonance observable, to a recognition or targeting moiety. Many contrast agents operate by affecting the relaxation properties of exchanging water, a concentrated solvent. The effect on relaxation can take place either passively, in which case the contrast agents are simply targeted to interesting sites, or be switched on upon binding to a dilute analyte. A recent innovation involves the use of paramagnetic lanthanides to generate a distinct resonance corresponding to the bound pool of the exchanging water, bringing the chemical exchange saturation transfer contrast mechanism under spectroscopic control [2]. Operating on similar principles, xenon-based molecular sensors are targeted, xenon-binding, host–guest complexes that reversibly bind xenon, generating a spectrally distinct species that can perturb the signal of hyperpolarized xenon gas dissolved in a bulk aqueous phase [3].

According to these principles, the ideal magnetic resonance contrast agent should operate like a transistor, amplifying a small signal (the analyte) in a controlled and linear way by proportionally perturbing a larger signal (the solvent or other abundant medium) over a wide dynamic range. Xenon-based molecular sensors fulfill these requirements, due primarily to several favorable properties of xenon itself. First, xenon has a very large chemical shift range due to the high polarizability of its electrons [4]. Consequently, one can selectively perturb either the population of xenon in bulk solvent or that encapsulated by a host sensor molecule [3,5] with high specificity [6]. Further, in most cases, xenon exchanges rapidly between the cage-bound and free forms, making sensitivity enhancements by chemical exchange saturation transfer (CEST, [7–10]) possible [11,12]. Because the chemical shift range of xenon is large, many targeted analytes can be distinguished by frequency changes resulting from minor chemical alterations to the host molecule [13,14]. Finally, xenon is hyperpolarizable by spin-exchange optical pumping [15], is chemically and biologically inert, and is water soluble. Recently, we have demonstrated that sub-picomolar concentrations of a novel xenon sensor construct can be detected within 20 s of saturation transfer [16].

In the above examples, the xenon chemical sensor contains the cage-like molecule cryptophane, a member of a class of small, organic structures that act as a host for xenon [17]. The conjugation

* Corresponding author at: Materials Sciences Division, Lawrence Berkeley National Laboratory, Berkeley, CA 94720, USA. Fax: +1 510 666 3768.
E-mail address: vikbajaj@gmail.com (V.S. Bajaj).

1090-7807/$ - see front matter © 2011 Elsevier Inc. All rights reserved.
doi:10.1016/j.jmr.2011.06.027

of these cages with chemical targeting units, including small molecules and peptides, is now routine [6]. When xenon is dissolved into a solvent that contains sensor in sufficiently high concentration, three peaks appear in the Xe NMR spectrum: a solvent peak ($Xe_{solvent}$), at ~190 ppm in aqueous solutions, a gas peak (Xe_{gas}) that is conventionally referenced to 0 ppm, and a peak corresponding to xenon encapsulated in the host cage (Xe@cage). The Xe@cage frequency depends strongly on the chemical composition of the cage subunit, but is usually between 30 and 70 ppm [18]. When a xenon cage sensor binds the analyte to which it is targeted, a fourth resonance appears ($Xe@cage_{bound}$), though it may be impossible to detect without chemical exchange-based amplification. A resonance corresponding to this bound form of the sensor is a significant and differentiating feature of xenon-based molecular imaging experiments.

Most useful work with xenon-based molecular sensors is conducted at low sensor concentrations (micromolar), precluding direct detection of the Xe@cage peak. Further, many relevant bound analytes will be found in micromolar or lower concentrations, so it is generally impossible to directly detect the bound resonance. Instead, the presence of these spectroscopic species is established using indirect detection experiments that use Hyper-CEST [12]. In Hyper-CEST experiments, a saturating radiofrequency field is applied at the Xe@cage or $Xe@cage_{bound}$ frequency, causing, over time, depletion of the $Xe_{solvent}$ signal with which xenon is exchanging. The normalized intensity in the presence of saturation is a contrast parameter that is related to the concentration of the probed species.

To date, xenon-based Hyper-CEST experiments have been conducted with strong continuous wave (CW) radiofrequency fields for frequency-selective saturation. There are several limitations with this approach. First, such experiments must be designed such that the saturation field perturbs only the desired resonance and not others, a task that is complicated by the strong dependence of saturation bandwidth on the saturation power. Hyper-CEST saturation transfer is optimized for CW pulse powers that result in partial saturation of the $Xe_{solvent}$ resonance, necessitating a second reference experiment and the use of kinetic modeling for quantification of the analyte. Further, multiplexing with xenon-based molecular sensors, a technique to resolve multiple variants of the sensor simultaneously [3], relies on small frequency separations between xenon bound in slightly different host molecules, precluding the use of broad saturation pulses. A related problem involves the spatial multiplexing of arrays of xenon chemical assays on, for example, a microfluidic device; in that case, the optimum imaging approach might involve spectral–spatial selective saturation [19] or multispectral saturation pulses with Hadamard encoding [20]. Finally, the time-averaged sensitivity of these experiments depends on highly efficient saturation, but is constrained *in vivo* by limits on the specific absorption rate (SAR) of the applied pulses [21]. These constraints cannot be simultaneously satisfied in CW-based saturation experiments.

To address these concerns, we have applied band-selective saturation pulse trains in lieu of CW pulses ordinarily used in Hyper-CEST experiments. These pulses have much greater frequency selectivity than CW pulses, relaxing the conditions needed for separate control experiments. They deliver comparable saturation efficiency at much lower powers, but, depending on the choice of pulse, allow for narrow-bandwidth saturation at high pulse powers. Finally, they are compatible with slice selection and therefore with imaging sequences that depend on spatial–spectral preparation or multispectral excitation or saturation. We demonstrate the application of these saturation pulses to both spectroscopy and imaging experiments employing xenon-based molecular sensors.

2. Results and discussion

2.1. Bloch simulations of frequency-selective saturation

Preliminary to our experimental investigation of saturation transfer phenomena in solutions of xenon molecular exchange agents, we conducted Bloch equation simulations of CW and multiple pulse saturation. These simulations involved numerical solution of the Bloch equations for an exchanging spin system subject to RF irradiation of a chosen amplitude profile. The simulation took relaxation and other parameters as defined by the experimental measurements and explored parameters including pulse bandwidth, B_1 amplitude, saturation time, and residence time of xenon in the cryptophane-xenon complex. Because xenon binding kinetics are not known accurately from our measurements or others (though

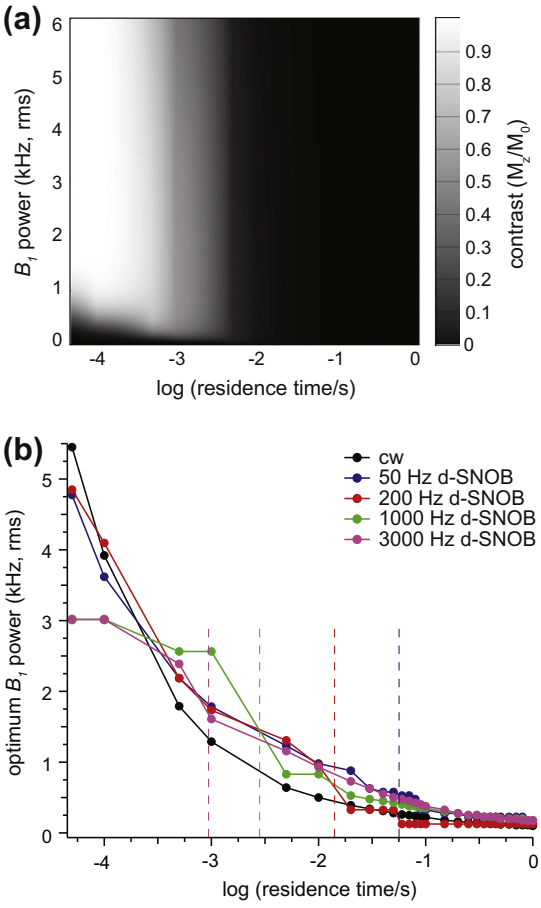

Fig. 1. Bloch equation simulations indicating contrast generated by various saturation parameters. (a) A contour plot illustrating the contrast generated by a CW pulse with various saturation powers, B_1, and on exchanging systems with difference residence times. Black indicates no contrast, while white indicates 100% contrast between an on-resonance experiment, in which the saturation is applied at the frequency of the exchanging species (Xe@cage), and an off-resonance experiment, in which the saturation is applied at a frequency equally distant from the Xe_{aq} resonance, but opposite of the Xe@cage resonance. Contour plots for d-SNOB saturation pulses are visually comparable to the one shown here. (b) The best contrast is not necessarily generated by saturation pulses with the highest power; rather, the saturation pulse power for optimum contrast depends strongly on the residence time of the guest in the host. Five different saturation pulses were simulated (CW, and four d-SNOB pulses with bandwidths of 50, 200, 1000, and 3000 Hz) for a range of residence times from 50 μs to 1 s. For each pulse, the power for optimum contrast decreases with increasing residence time. While the CW pulse shows primarily exponential behavior, the d-SNOB pulses have irregular behavior, including discontinuities in the power-residence time curve. The vertical dashed lines indicate the length of time each unique d-SNOB pulse lasts. All simulation parameters are provided in Supporting Information.

estimated to be 5–50 ms, depending on temperature, concentration, and solvent), these simulations are merely a guide to the parameter space, and not a rigorous route to optimal saturation parameters. Nevertheless, they reveal several important trends. In Fig. 1, we present plots that relate the observed saturation to B_1 field and residence time (inverse of the exchange rate). For CW saturation, the power at which optimum saturation is obtained decreases exponentially with increasing residence time. The functional dependence for multiple pulse sequences based on d-SNOB elements is non-exponential and, at high pulse bandwidths, is characterized by an initial region in which the power dependence is approximately flat. Fig. 2 illustrates this trend, showing that in the optimal case, multiple pulse saturation performs better than CW saturation for a range of relevant residence times. However, the powers at which these optimal saturations are achieved can be up to an order of magnitude higher for CW saturation.

2.2. Saturation of water

To determine the effective saturation bandwidth for CW pulses of different powers, we applied them to an aqueous solution of 1 mM gadolinium coordinated with diethylene triamine pentaacetic acid (Gd–DTPA), a concentration of paramagnetic dopant which yielded a proton T_1 of approximately 1 s and which was selected purely for experimental convenience. Each saturation pulse was applied at frequencies ranging from +5 kHz to −5 kHz of the ^{1}H resonance frequency. The strength of the applied field, B_1, was varied between 15 and 950 Hz. A contour plot of these saturation data is provided in Fig. 3. For the highest pulse powers, saturation of 10% or more of the water signal extends ±3 kHz from the ^{1}H resonance frequency, corresponding to roughly a 70 ppm range at an external magnetic field strength B_0 = 7.05 T. The contrast in xenon sensor experiments may be one order of magnitude lower (∼1%) for the lowest detectable concentrations.

We examined the properties of several shaped pulses for band-selective saturation—a Gaussian inversion pulse [22], a SEDUCE pulse [23], and a d-SNOB pulse [24]. We did not explore Guassian-sinc convolution pulses or pulses obtained through the Shinnar-Le Roux procedure [25,10]. In our saturation experiments using the 1 mM Gd–DTPA aqueous solution, pulses calculated to have 50 Hz and 200 Hz bandwidth at canonical power levels were

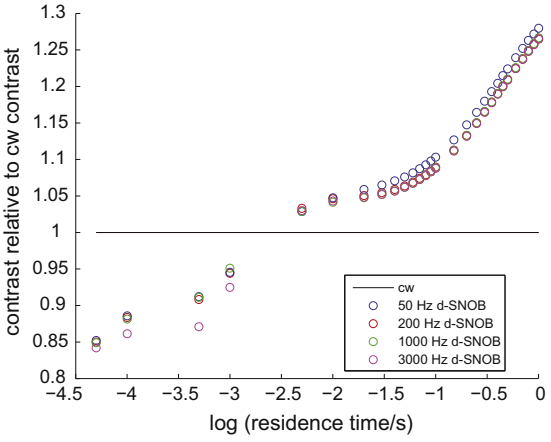

Fig. 2. A comparison of the simulated contrast generated by power-optimized d-SNOB pulses relative to a CW pulse acting under the same conditions. The best contrast for each pulse at each exchange time was selected and normalized to the CW contrast at that point. At exchange times of approximately 2.5 ms, all d-SNOB saturation pulses can generate more contrast than CW pulses, with the improvement increasing with longer residence times. All simulation parameters are provided in Supporting Information.

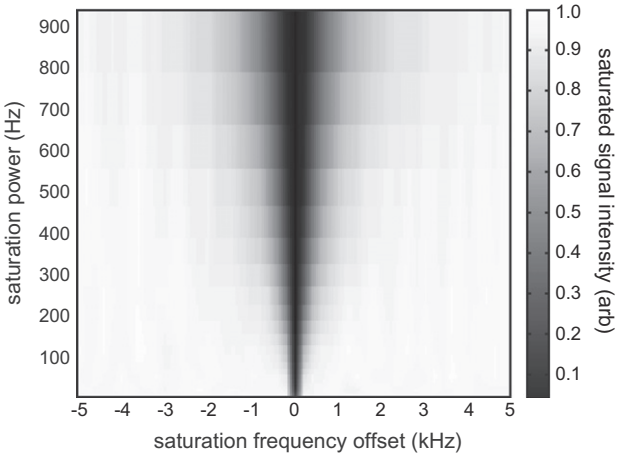

Fig. 3. Effective bandwidth of CW saturation of water. Continuous wave pulses of varying applied field strengths B_1 were applied at frequencies ±5 kHz from the ^{1}H resonance frequency of an aqueous sample of 1 mM Gd-DTPA for 500 ms each. Black shading indicates complete saturation of the water signal. As the CW pulse power is increased, the effective bandwidth of saturation increases—at $B_1 \approx 900$ Hz, 10% or more of the signal is saturated over a bandwidth of ∼6 kHz.

used. Each pulse pattern was repeated without any inter-pulse delays for the duration of the saturation period. The saturation profile for each of these pulses is shown in Fig. 4. Despite a slightly longer pulse duration and higher power deposition than the Gaussian and SEDUCE pulses, the d-SNOB pulse provides the most efficient saturation with the narrowest effective bandwidth. For the 200 Hz d-SNOB pulse, 90% saturation extended ±325 Hz from the center frequency with only 15% or less saturation outside of the desired bandwidth; for the 50 Hz d-SNOB pulse, 90% saturation extended ±75 Hz from the center frequency with only 20% or less saturation outside of the desired bandwidth. We investigated the effects of the pulse phase supercycle MLEV-4 on the saturation profile [26] and found them to be insignificant for this arrangement of hardware and sample. Consequently, we did not rigorously investigate the effect of phase supercycles on exchanging xenon systems. Finally, because our goal was primarily to compare CW saturation transfer to multiple pulse saturation sequences, we decided to investigate only a small subset of the many similar pulse shapes that might be used as building blocks of other saturation pulse trains. Parameters for all pulses are detailed in figure captions.

2.3. Saturation of ^{129}Xe

We performed similar saturation experiments on an aqueous solution of a cage-like xenon host molecule, cryptophane-A, and observed chemical exchange saturation transfer. The cage, modified to bear an acetate group as a chemical handle for covalent functionalization, was conjugated to the pentapeptide EEEEK to increase the aqueous solubility of the molecule [27]; the solutions used in these experiments had a cage concentration of 50 μM. Hyperpolarized xenon was bubbled into the cage solution prior to each acquisition. At external field strength B_0 = 7.05 T, the frequency corresponding to xenon in cage (Xe@cage) is approximately 11 kHz upfield of the resonance of xenon dissolved in water (Xe_{aq}). Saturation profiles were collected by applying both d-SNOB and Gaussian pulses at frequencies near the Xe@cage frequency; the SEDUCE pulse was not tested because of its larger saturation bandwidth in the control experiments using water.

For comparison of the effective saturation bandwidth, two CW pulses of different applied powers (low power, B_1 = 113 Hz; high-power, B_1 = 449 Hz) were applied at the Xe@cage frequency, as shown in Fig. 5. The CW pulses showed 90% or more saturation

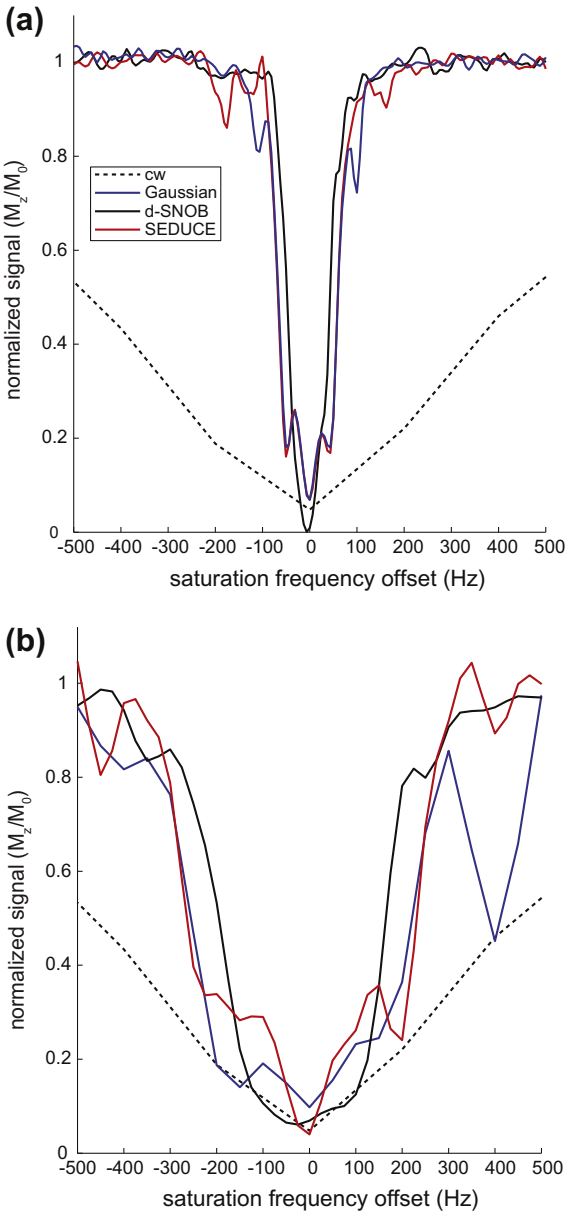

Fig. 4. Effective saturation bandwidth for shaped and CW saturation pulses in water with frequency offsets relative to the ^{1}H resonance frequency. The CW pulse was applied for 500 ms with an applied field strength B_1 = 498 Hz. (a) 50 Hz Gaussian (18.0 ms, $B_{1,peak}$ = 70.3 Hz, 900 ms total saturation time), d-SNOB (56.4 ms, $B_{1,peak}$ = 62.6 Hz, 564 ms total saturation time), and SEDUCE (17.25 ms, $B_{1,peak}$ = 62.6 Hz, 431 ms total saturation time) pulses show at least 10% saturation of the water signal in an aqueous solution of 1 mM Gd-DTPA over ~200 Hz. (b) 200 Hz Gaussian (4.5 ms, $B_{1,peak}$ = 314 Hz, 225 ms total saturation time), d-SNOB (14.1 ms, $B_{1,peak}$ = 249 Hz, 423 ms total saturation time), and SEDUCE (4.31 ms, $B_{1,peak}$ = 249 Hz, 129 ms total saturation time) pulses show at least 10% saturation of the water signal in the same solution over >600 Hz. The rms power of a d-SNOB pulse is approximately 50% of the peak power.

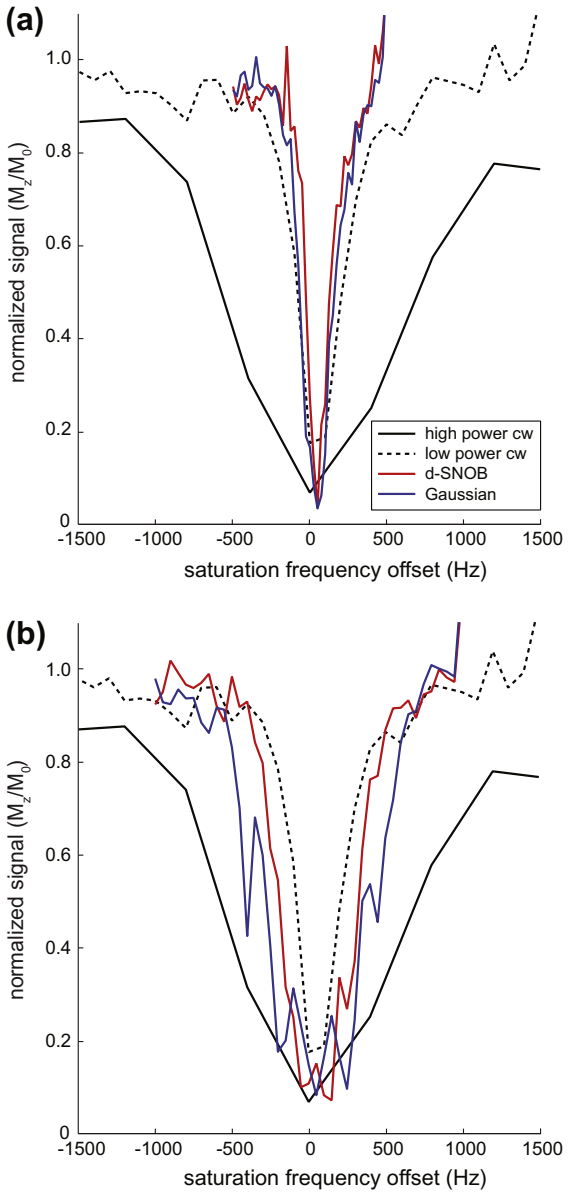

Fig. 5. Effective saturation bandwidth for shaped and CW saturation pulses in the solution containing hyperpolarized ^{129}Xe and cryptophane-A. Offsets are relative to the Xe@cage resonance frequency. For comparison, two CW pulses are shown: a low-power pulse (B_1 = 113 Hz, 1.5 s saturation) and a high-power pulse (B_1 = 449 Hz, 2.0 s). (a) 50 Hz Gaussian (18.0 ms, $B_{1,peak}$ = 80.0 Hz, 2.52 s total saturation time) and d-SNOB (56.4 ms, $B_{1,peak}$ = 63.3 Hz, 2.26 s total saturation time) pulses show at least 10% saturation of the Xe_{aq} signal in an aqueous solution of 50 μM cryptophane-A over >475 Hz. (b) 200 Hz Gaussian (4.5 ms, $B_{1,peak}$ = 318 Hz, 1.35 s total saturation time) and d-SNOB (14.1 ms, $B_{1,peak}$ = 252 Hz, 1.13 s total saturation time) pulses show similar saturation over >1000 Hz. The rms power of a d-SNOB pulse is approximately 50% of the peak power.

within bandwidths of 5800 Hz and 1200 Hz for high and low power, respectively. In contrast, the 200 Hz bandwidth pulses showed 90% or more saturation within bandwidths of 1300 Hz (Gaussian) and 1000 Hz (d-SNOB); the 50 Hz bandwidth pulses showed 90% or more saturation within bandwidths of 475 Hz (Gaussian) and 1275 Hz (d-SNOB). The results of these experiments are also shown in Fig. 5. We note that saturation transfer is optimized when these sequences are applied slightly off-resonance (~125 Hz) from the expected Xe@cage resonance frequency. In addition, as illustrated in Fig. 6, multiple pulse saturation sequences can generate similar or even more contrast than can CW pulses at a lower average power level.

We next demonstrated the utility of band-selective saturation transfer in an exchanging xenon sensor system subject to homogeneous and inhomogeneous broadening. This conjugate, MS2CA, is an engineered nanoparticle in which ~125 cryptophane cages have been covalently attached to an MS2 viral capsid scaffold [16]. The capsid surface has 32 pores, each 2 nm in diameter, through which solvent exchanges in and out of the capsid. The resulting particle inherits all the favorable properties of the viral capsid, including biocompatibility, stability, and host targeting, and so is important

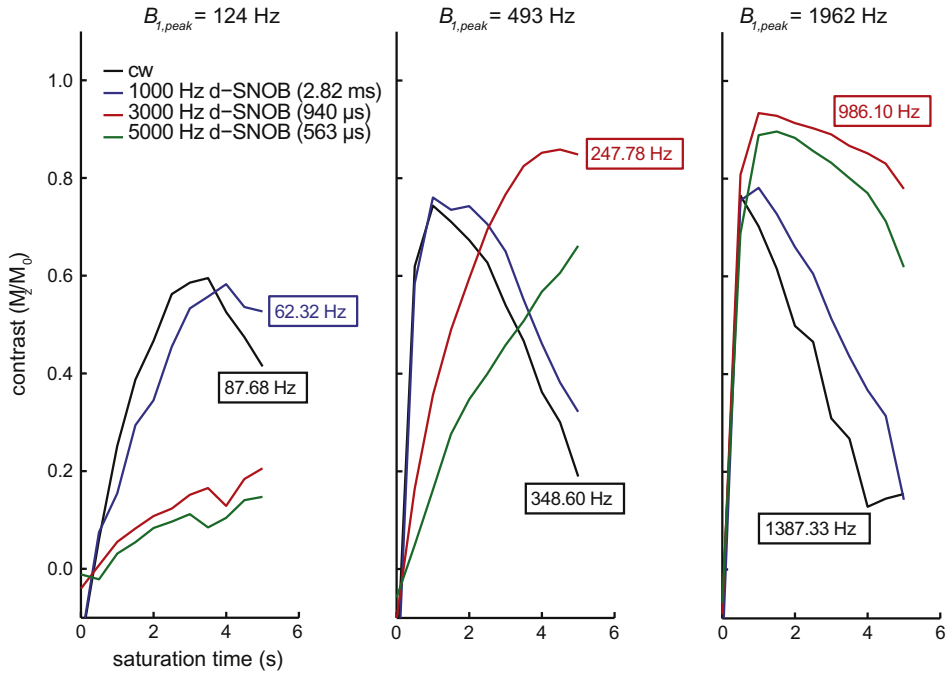

Fig. 6. Experimental results showing the contrast generated using CW and d-SNOB pulses at different pulse powers. At lower pulse powers, lower bandwidth d-SNOB (1000 Hz bandwidth) and CW pulses provide the best contrast, while at higher powers, shorter d-SNOB pulses (3000 and 5000 Hz bandwidth) provide the greatest contrast. Saturation was applied on-resonant to a sample of 70 μM CryA in benzyl alcohol at the peak power B_1 and saturation time indicated. The rms power of the CW pulse is 70.7% of the peak power, and the rms power of the d-SNOB pulses is 50.3% of the peak power; the rms power for both CW and d-SNOB pulses is indicated in the boxes.

in our effort to use xenon molecular sensors for *in vivo* bioimaging. We used a 7 nM solution of MS2CA (assembled capsids, corresponding to 900 nM cryptophane-A cages). To this solution, we applied saturation pulses, both CW and d-SNOB (100 Hz bandwidth), incrementally varying the frequency to measure saturation transfer spectra. Collected at frequencies between the Xe_{aq} and Xe@cage resonances, these indirectly detected spectra are shown in Fig. 7.

When optimized, the saturation transfer contrast under CW irradiation at the Xe_{aq} frequency was comparable to that resulting from the d-SNOB saturation; however, the d-SNOB saturation required much less power and a shorter saturation time—the total power deposited with the d-SNOB pulses was approximately 30 times less than that deposited with the CW pulse. In addition, the resolution of the indirectly detected spectrum is superior, as evidenced by the visibility of the baseline between the Xe_{aq} and Xe@cage peaks in the d-SNOB spectrum.

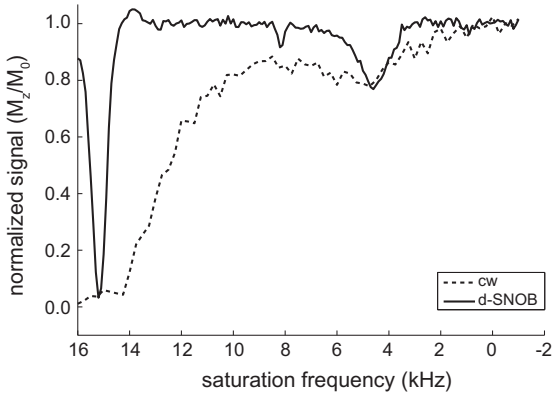

Fig. 7. The resolution of a *Z*-spectrum showing magnetization transfer after saturation is greatly improved by using frequency selective d-SNOB pulses. The *z*-spectra collected with both CW (B_1 = 622 Hz, 20 s saturation) and d-SNOB (100 Hz bandwidth, $B_{1,peak}$ = 78.3 ms, 10.2 s total saturation) show comparable saturation of both the Xe_{aq} peak (~15 kHz) and the Xe@cage peak (~4 kHz). However, only in the d-SNOB *Z*-spectrum is the baseline between the two resonances clearly discernible. Furthermore, the d-SNOB saturation sequence deposits approximately 30 times less power into the sample than does CW saturation. A feature at ~8 kHz saturation frequency is reproducible in all MS2 preparations, and its source is presently under investigation.

2.4. Hyper-CEST imaging experiments

To demonstrate the utility of these frequency selective saturation pulses in saturation transfer imaging, we conducted prototype imaging experiments on a simple system placed in a one-dimensional gradient for excitation and detection of one-dimensional images. Specifically, we placed two 10-mm NMR tubes ("phantoms") adjacent to one another in a 30-mm probe, as shown schematically in Fig. 8a. The solvent in both phantoms was benzyl alcohol to increase the solubility of both xenon and cryptophane-A. The left phantom (#1) contained 0.5 mM cryptophane-A while the right phantom (#2) contained none. The spectra are excited and detected in the presence of a linear magnetic field gradient to produce a one-dimensional image of the phantom. Fig. 8b shows a one-dimensional ^{129}Xe NMR profile, verifying separation between the two phantoms. We applied a series of 200 Hz bandwidth d-SNOB pulses at various points in the spectrum as shown in Fig. 8c–h. When saturation was applied at the frequency corresponding to xenon dissolved in benzyl alcohol ($Xe_{solvent}$), a hole was burned into the profile of the appropriate phantom (Fig. 8c and d). When saturation was applied at the Xe@cage frequency (11 kHz upfield of the $Xe_{solvent}$ frequency) a hole was burned into the profile of phantom #1, which contained cryptophane-A, but not into that of phantom #2. To verify that the hole burning in the above experiments was not due to direct saturation of the $Xe_{solvent}$ peak, we applied off-resonant saturation pulses at frequencies 11 kHz downfield of the $Xe_{solvent}$ resonances (Fig. 8g and h). Neither off-resonant case showed saturation of the ^{129}Xe signal. We therefore anticipate that these band-selective saturation

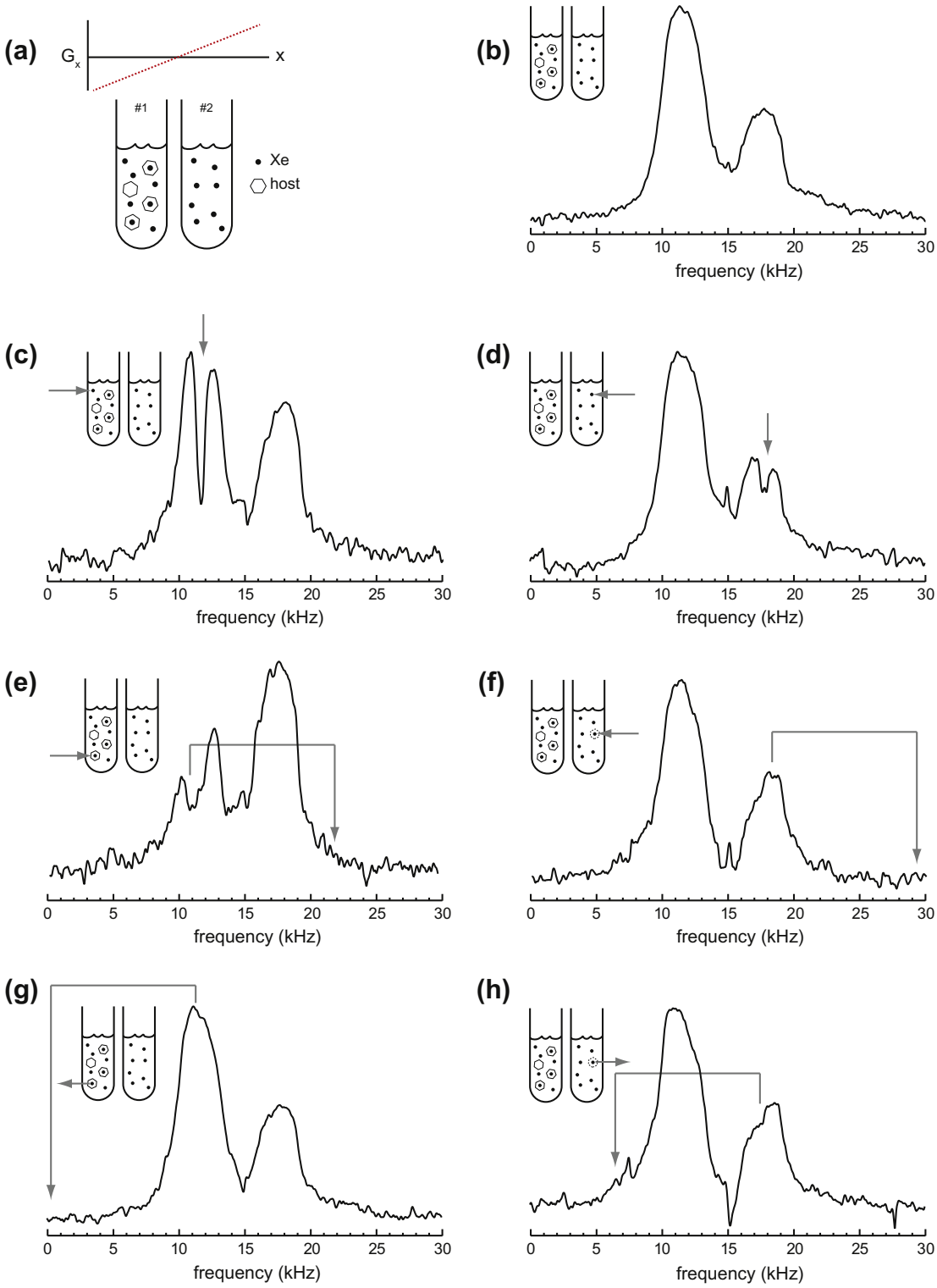

Fig. 8. Frequency selective saturation transfer pulses applied to imaging. (a) The apparatus consists of two 10-mm NMR phantoms side-by-side in a 30 mm probe. Both phantoms are filled with benzyl alcohol to increase the solubility of both xenon and the xenon host molecule cryptophane-A. The left phantom (#1) contains both xenon and cryptophane-A while the right phantom (#2) contains only xenon. The spectra are detected in the presence of a linear magnetic field gradient to produce a one-dimensional image. (b) A one-dimensional profile of the two phantoms. The difference in intensity is due to a mismatch in the delivery of hyperpolarized xenon to the two phantoms. (c and d) Saturation applied directly at the $Xe_{solvent}$ frequencies results in hole burning in the profiles of both phantoms. (e and f) Applying saturation at a frequency 11 kHz upfield of the $Xe_{solvent}$ resonance, corresponding to the Xe@cage resonance, shows saturation only in phantom #1 (e) where cryptophane-A is present. Phantom #2 (f), not containing cryptophane-A, shows no saturation. (g and h) To verify that saturation results from magnetization transfer through chemical exchange of xenon and not from direct saturation of the $Xe_{solvent}$ resonance, saturation pulses are applied 11 kHz downfield of the $Xe_{solvent}$ resonances. No saturation is observed in either phantom, indicating that the saturation observed in (e) is a result of Hyper-CEST saturation transfer. The vertical scale is not constant for (b) through (h).

transfer sequences can form the basis of spectral–spatial selective imaging or Hadamard imaging schemes based on multispectral excitation.

3. Conclusion

We have demonstrated that band-selective saturation sequences allow independent optimization of the parameters governing chemical shift saturation transfer experiments. The selectivity and efficiency of saturation using the sequences demonstrated above is superior to conventional approaches based on CW radiation, and the effective bandwidth of saturation is tunable over a wide range by manipulating the pulse duration and power. While we have only examined d-SNOB and Gaussian pulse trains for xenon systems, it is possible that other sequences based on rotating frame saturation or dephasing will yield superior results. In addition, the power required to achieve saturation with these shaped pulses is significantly reduced, which may be relevant in applications where specific absorption rate (SAR) limitations become limiting. Alternatively, in experiments *in vitro* in which SAR is not limiting, new detection thresholds for xenon-based molecular sensors may be achieved by generating more saturation per time in the magnetization transfer system. Such sequences may also form the building blocks of imaging methods that require simultaneous control over the spectral and spatial extent of saturation, or those which require saturation at multiple simultaneous frequencies. We did not explore applications to conventional CEST contrast agents here but anticipate that similar considerations will apply in those experiments.

4. Experimental

All experiments were performed using a 7.05 T NMR spectrometer (Varian Inc., Palo Alto, CA) with 5 mm (saturation profiles, MS2CA) and 30 mm (imaging) probes. The imaging probe was highly optimized for xenon performance at the expense of performance on the ^{1}H channel. Imaging experiments were conducted using a gradient coil assembly (Resonance Research Inc., Billerica, MA) for spatial encoding. For the one-dimensional profiles, the applied gradient field strength was $G = 3.4\ \mathrm{G\ cm^{-1}}$. Gaussian, SEDUCE, and d-SNOB pulse profiles were generated using the default pulse profiles and the "pxshape" tool in the VNMR software package (Varian Inc.). Each pulse was checked for proper behavior, either excitation or inversion, and the pulse power was adjusted by up to ±1 dB accordingly. Individual pulse durations and powers are given in appropriate figure captions.

Hyperpolarized ^{129}Xe ($P \approx 4\%$) was generated with a XenoSpin polarizer (Amersham Health, Durham, NC) using a mixture of 1% (saturation profiles) or 2% (MS2CA, imaging) xenon (natural abundance ^{129}Xe), 10% N_2, and the balance He (Airgas, Radnor, PA). Xenon was delivered to the NMR phantoms using a bubbling setup as previously described [28]. When performing imaging experiments, the xenon delivery system was modified to deliver pressurized gas to two phantoms simultaneously. For the saturation profile experiments, xenon was bubbled into the phantoms at ~70 psi pressure for 10 s at 0.35 standard liters per minute (SLM), followed by a 1 s stopped-flow delay to allow dissipation of bubbles in the phantom prior to acquisition. For experiments involving MS2CA, xenon was bubbled at ~70 psi pressure for 20 s at 0.3 SLM, followed by a 4 s settling delay prior to acquisition. For imaging experiments, xenon was bubbled at ~60 psi pressure for 10 s at 0.65 SLM, followed by a 2 s settling delay prior to acquisition.

For xenon experiments involving saturation profiles and the MS2CA conjugate, the Xe@cage resonance was not directly visible in the spectra. Consequently, the Xe@cage frequency was found by incrementally varying the frequency of a saturation pulse in the region between the $Xe_{solvent}$ resonance and the Xe_{gas} resonance (0 ppm) and monitoring saturation transfer to the $Xe_{solvent}$ signal. Using this method, the frequency of the Xe@cage resonance was determined to an accuracy of ±25 Hz (saturation profiles) or ±50 Hz (MS2).

For each acquisition, the appropriate excitation pulse was followed by an acquisition time of 1 s (^{1}H experiments), 500 ms (xenon saturation profiles), 200 ms (MS2), or 100 ms (xenon imaging). Four transients were collected for xenon saturation profiles and for imaging experiments. Post-processing was performed in NMRPipe [29] and included the application of an apodization filter and zero-filling prior to Fourier transformation. Integration and normalization of the $Xe_{solvent}$ peak area for *z*-spectra was done using MATLAB® (The MathWorks Inc., Natick, MA).

Acknowledgment

This research was supported by the US Department of Energy, Office of Basic Energy Sciences, Division of Materials Sciences and Engineering under Contract No. DE-AC02-05CH11231. We acknowledge the generous and unrestricted support of the Agilent Foundation, Chevron Energy, and Schlumberger-Doll Research.

Appendix A. Supplementary material

Supplementary data associated with this article can be found, in the online version, at doi:10.1016/j.jmr.2011.06.027.

References

[1] H. Lee, T. Yoon, R. Weissleder, Ultrasensitive detection of bacteria using core–shell nanoparticles and a NMR-filter system, Angew. Chem. Int. Ed. 48 (2009) 5657–5660.
[2] M. Woods, D. Woessner, A. Sherry, Paramagnetic lanthanide complexes as PARACEST agents for medical imaging, Chem. Soc. Rev. 35 (2006) 500–511.
[3] M.M. Spence, S.M. Rubin, I.E. Dimitrov, E.J. Ruiz, D.E. Wemmer, A. Pines, S.Q. Yao, F. Tian, P.G. Schultz, Functionalized xenon as a biosensor, Proc. Natl. Acad. Sci. 98 (2001) 10654–10657.
[4] K.W. Miller, N.V. Reo, A.J.M. Schoot Uiterkamp, D.P. Stengle, T.R. Stengle, K.L. Williamson, Xenon NMR: chemical shifts of a general anesthetic in common solvents proteins and membranes, Proc. Natl. Acad. Sci. 78 (1981) 4946–4949.
[5] C. Hilty, T.J. Lowery, D.E. Wemmer, A. Pines, Spectrally resolved magnetic resonance imaging of a xenon biosensor, Angew. Chem. Int. Ed. 45 (2006) 70–73.
[6] M.M. Spence, E.J. Ruiz, S.M. Rubin, T.J. Lowery, N. Winssinger, P.G. Schultz, D.E. Wemmer, A. Pines, Development of a functionalized xenon biosensor, J. Am. Chem. Soc. 126 (2004) 15267–15294.
[7] P.M. Jacquart, L. Roux, Influence of the electrical resistivity of a ferromagnetic thin film on its permeability measurement performed with a permeameter, J. Magn. Magn. Mater. 281 (2004) 82–91.
[8] C.H. Cunningham, M.L. Wood, Method for improved multiband excitation profiles using the Shinnar-Le Roux transform, Magn. Reson. Med. 42 (1999) 577–584.
[9] V.N. Ikonomidou, G.D. Sergiadis, Improved Shinnar-Le Roux algorithm, J. Magn. Reson. 143 (2000) 30–34.
[10] K.J. Lee, General parameter relations for the Shinnar-Le Roux pulse design algorithm, J. Magn. Reson. 186 (2007) 252–258.
[11] K. Ruppert, J. Brookeman, K. Hagspiel, J. Mugler III, Probing lung physiology with xenon polarization transfer contrast (XTC), Magn. Reson. Med. 44 (2000) 349–357.
[12] L. Schröder, T.J. Lowery, C. Hilty, D.E. Wemmer, A. Pines, Molecular imaging using a targeted magnetic resonance hyperpolarized biosensor, Science 314 (2006) 446–449.
[13] G. Huber, T. Brotin, L. Dubois, H. Desvaux, J.-P. Dutasta, P. Berthault, Water soluble cryptophanes showing unprecedented affinity for xenon: candidates as NMR-based biosensors, J. Am. Chem. Soc. 128 (2006) 6239–6246.
[14] B.S. Kim, Y.H. Ko, Y. Kim, H.J. Lee, N. Selvapalam, H.C. Lee, K. Kim, Water soluble cucurbit [6] uril derivative as a potential Xe carrier for Xe-129 NMR-based biosensors, Chem. Commun. (2008) 2756–2758.
[15] T. Walker, W. Happer, Spin-exchange optical pumping of noble-gas nuclei, Rev. Mod. Phys. 69 (1997) 629–642.
[16] T. Meldrum, K.L. Seim, V.S. Bajaj, K. Palaniappan, W. Wu, M.B. Francis, D.E. Wemmer, A. Pines, A xenon-based molecular sensor assembled on an MS2 viral capsid scaffold, J. Am. Chem. Soc. 132 (2010) 5936–5937.

[17] J. Gabard, A. Collet, Synthesis of a (D 3)-Bis (cyclotriveratrylenyl) macrocage by stereospecific replication of a (C 3)-subunit, J. Chem. Soc. Chem. Commun. 1981 (1981) 1137–1139.
[18] T. Brotin, J. Dutasta, Cryptophanes and their complexes – present and future, Chem. Rev. 109 (2009) 88–130.
[19] C. Meyer, J. Pauly, A. Macovski, D. Nishimura, Simultaneous spatial and spectral selective excitation, Magn. Reson. Med. 15 (1990) 287–304.
[20] A. Tal, B. Shapira, L. Frydman, Single-scan 2D Hadamard NMR spectroscopy, Angew. Chem. Int. Ed. 48 (2009) 2732–2736.
[21] P. Röschmann, Radiofrequency penetration and absorption in the human body: limitations to high-field whole-body nuclear magnetic resonance imaging, Med. Phys. 14 (1987) 922–931.
[22] C. Bauer, R. Freeman, T. Frenkiel, J. Keeler, A. Shaka, Gaussian pulses, J. Magn. Reson. 58 (1984) 442–457.
[23] M.A. Mccoy, L. Mueller, Selective decoupling, J. Magn. Reson. Ser. A 101 (1993) 122–130.
[24] E. Kupce, J. Boyd, I. Campbell, Short selective pulses for biochemical applications, J. Magn. Reson. Ser. B 106 (1995) 300–303.
[25] M. Shinnar, L. Bolinger, J.S. Leigh, The use of finite impulse-response filters in pulse design, Magn. Reson. Med. 12 (1989) 81–87.
[26] M.H. Levitt, R. Freeman, T. Frenkiel, Broadband heteronuclear decoupling, J. Magn. Reson. 47 (1982) 328–330.
[27] L. Schröder, T. Meldrum, M. Smith, T.J. Lowery, D.E. Wemmer, A. Pines, Temperature response of Xe-129 depolarization transfer and its application for ultrasensitive NMR detection, Phys. Rev. Lett. 100 (2008) 257603(4).
[28] S.-I. Han, S. Garcia, T.J. Lowery, E.J. Ruiz, J.A. Seeley, L. Chavez, D.S. King, D.E. Wemmer, A. Pines, NMR-based biosensing with optimized delivery of polarized 129Xe to solutions, Anal. Chem. 77 (2005) 4008–4012.
[29] F. Delaglio, S. Grzesiek, G. Vuister, G. Zhu, J. Pfeifer, A. Bax, NMRPipe: a multidimensional spectral processing system based on UNIX pipes, J. Biomol. NMR 6 (1995) 277–293.